Lagrangian statistics across the turbulent-nonturbulent interface in a turbulent plane jet

Rodrigo R. Taveira, José S. Diogo, Diogo C. Lopes, and Carlos B. da Silva*
IDMEC/Instituto Superior Técnico, Technical University of Lisbon, Pav. Mecânica I, 1*º andar/esq./LASEF, Av. Rovisco Pais, 1049-001 Lisboa, Portugal*

(Received 23 April 2013; revised manuscript received 18 August 2013; published 8 October 2013)

Lagrangian statistics from millions of particles are used to study the turbulent entrainment mechanism in a direct numerical simulation of a turbulent plane jet at $\mathrm{Re}_\lambda \approx 110$. The particles (tracers) are initially seeded at the irrotational region of the jet near the turbulent shear layer and are followed as they are drawn into the turbulent region across the turbulent-nonturbulent interface (TNTI), allowing the study of the enstrophy buildup and thereby characterizing the turbulent entrainment mechanism in the jet. The use of Lagrangian statistics following fluid particles gives a more correct description of the entrainment mechanism than in previous works since the statistics in relation to the TNTI position involve data from the trajectories of the entraining fluid particles. The Lagrangian statistics for the particles show the existence of a velocity jump and a characteristic vorticity jump (with a thickness which is one order of magnitude greater than the Kolmogorov microscale), in agreement with previous results using Eulerian statistics. The particles initially acquire enstrophy by viscous diffusion and later by enstrophy production, which becomes "active" only deep inside the turbulent region. Both enstrophy diffusion and production near the TNTI differ substantially from inside the turbulent region. Only about 1% of all particles find their way into pockets of irrotational flow engulfed into the turbulent shear layer region, indicating that "engulfment" is not significant for the present flow, indirectly suggesting that the entrainment is largely due to "nibbling" small-scale mechanisms acting along the entire TNTI surface. Probability density functions of particle positions suggests that the particles spend more time crossing the region near the TNTI than traveling inside the turbulent region, consistent with the particles moving tangent to the interface around the time they cross it.

DOI: 10.1103/PhysRevE.88.043001 PACS number(s): 47.27.E−, 47.27.wg, 47.27.nb

I. INTRODUCTION

Turbulent entrainment designates a mechanism existing in many turbulent flows such as mixing layers, jets, wakes, and boundary layers and governs many key aspects of the flow development. The growth of shear layers, the speed of contaminants dispersion, and the mixing and reaction rates in turbulent combustion are some examples of processes largely governed by turbulent entrainment [1]. Turbulent entrainment is therefore of central importance to many natural and engineering flows.

In these flows a sharp and convoluted layer or interface—the turbulent-to-nonturbulent interface (TNTI)—separates the flow into two regions: (i) the shear layer region where the flow is turbulent and (ii) an irrotational or nonturbulent flow region [2]. Turbulent entrainment is the mechanism by which fluid parcels at the irrotational flow region acquire vorticity and become part of the turbulent region. The exchanges of mass, momentum and heat characterizing the entrainment take place across the TNTI, hence its importance in the context of the study of turbulent entrainment. It has been reported that some quantities display sharp jumps at the TNTI, e.g., the vorticity and mean streamwise velocity [3].

Despite its importance, many aspects of the turbulent entrainment are presently poorly understood. In particular, two different models have been advanced to explain the turbulent entrainment mechanism. According to the *engulfment model* [4], the entrainment proceeds in two stages: (i) an inviscid first stage, where large-scale eddy motions drag (by induced velocity) pockets of irrotational flow from the irrotational region into the core of the turbulent region, and (ii) a (viscous) diffusion second stage whereby these islands of irrotational flow slowly acquire vorticity. According to the *nibbling model* the entrainment happens by vorticity diffusion across the entire TNTI caused by nearby small-scale eddy motions [2]. Some recent experimental and numerical works suggest that "nibbling" is the dominating mechanism at least for jets [5,6]; however, there is yet no definitive answer for the question of whether "nibbling" or "engulfment" are the most important for the turbulent entrainment. Philip and Marusic [7] discuss how differences in large-scale eddies from jets, wakes, and shear free turbulence (i.e., turbulence without mean shear) imply a different relative importance of "nibbling" and "engulfing" in these flows.

The most distinctive feature between the flow regions separated by the TNTI consists in the strong contrast between the total absence of vorticity in the irrotational zone and the high vorticity content of the turbulent zone. It seems therefore natural to address the mechanisms behind the turbulent entrainment by analyzing the mechanisms by which the enstrophy is communicated to the irrotational flow region and several previous works have addressed this problem. Holzner *et al*. [8] analyzed the dynamics of the enstrophy transport equation in an experimental turbulent front generated by an oscillating grid at low Reynolds numbers. They observed the existence of positive viscous vorticity effects at the TNTI, promoting an increase in the local enstrophy. Subsequently, da Silva and Pereira [9] and Holzner *et al*. [10] observed that this enstrophy increase is caused by viscous diffusion effects, while viscous dissipation remains negative throughout the whole turbulent region. Da Silva and Reis [11] analyzed the

*carlos.silva@ist.utl.pt

 ©2013 American Physical Society

role of coherent vortices near the TNTI and observed that large vorticity structures near the TNTI are responsible for the existence of positive enstrophy diffusion along this layer, linking the results of Holzner *et al*. [8,10] to the large-scale vorticity structures. Moreover da Silva *et al*. [12] analyzed the dynamics of the small-scale intense vorticity structures at the TNTI. The results suggest that the "nibbling" eddy motions are linked with the diffusion of vorticity from these small-scale vortices at the TNTI. However, the large-scale eddies definitively play an important role on the dynamics of the entrainment, as shown in, e.g., Cortesi *et al*. [13], where the effects of stratification and thermal conductivity were assessed.

The goal of the present work is to study the enstrophy dynamics across the TNTI in order to shed light on the dynamics of the turbulent entrainment mechanism. For this purpose a direct numerical simulation (DNS) of temporally evolving planar jet was used. In addition to the Navier-Stokes simulation, millions of particles (tracers) were tracked during the simulation. The particles were initially placed in the irrotational region near the TNTI and *Lagrangian statistics* were computed for the particles that crossed the TNTI into the turbulent region, allowing for a detailed study of the buildup of vorticity for the entrained particles. The tracked particle trajectories were used also to assess the relative importance of the "nibbling" or "engulfment" mechanisms in the jet. Compared to previous studies, the use of Lagrangian statistics reported in the present work gives a more correct description of the entrainment mechanism since these statistics use trajectories of particles in the process of being entrained into the jet.

This article is organized as follows. In Sec. II we describe the temporal turbulent planar jets DNS used in the present work, along with the procedure employed to compute the statistics. Section III analyzes evolution of the enstrophy for the entrained particles during the simulation, and Sec. IV uses the particle trajectories to assess the relative importance of the "engulfment" mechanism for the present simulation. The work ends with an overview of the main results and a summary of the main conclusions (Sec. V).

II. DIRECT NUMERICAL SIMULATION OF A TURBULENT PLANE JET

A DNS of a turbulent plane jet is used in the present work. The simulation is one of the simulations used before and described in detail in da Silva and Taveira [14] (labelled $\text{PJET}_{\text{chan.}}$) and therefore only a short description will be give here.

A. Numerical method

The Navier-Stokes solver employs pseudospectral methods for spatial discretization and a three-step Runge-Kutta scheme for temporal advancement. The initial conditions consist of interpolated velocity fields from a DNS of a turbulent channel flow and the initial Reynolds number is equal to $\text{Re}_H = U_1 H/\nu = 3200$, where U_1 is the maximum initial (mean) stream-wise velocity. The simulations were halted before any effect of the boundary conditions could be observed in the jet statistics, e.g., the Reynolds stresses.

B. Physical and computational parameters

The computational domain extends to $(L_x, L_y, L_z) = (6.3H, 6H, 4.2H)$ along the streamwise (x), normal (y), and spanwise (z) jet directions, respectively, and the simulation uses $(N_x \times N_y \times N_z) = (384 \times 486 \times 384)$ grid points. The simulation was fully dealiased using the 2/3 rule.

One point statistics and spectra showed that the present DNS is accurate at the large and small scales of motion and representative of a fully developed turbulent plane jet [14]. Specifically, the mean streamwise velocity profile and Reynolds stresses profiles agree well with the data available and the computational box is big enough and does not constrain the jet in its development. For this DNS the self-similar regime is obtained at $t/t_{\text{ref}} \approx 20$, where $t_{\text{ref}} = H/(2U_1)$ and at this stage the Reynolds number based on the Taylor microscale λ, and the root-mean-square of the streamwise velocity u' is equal to $\text{Re}_\lambda = u'\lambda/\nu \approx 110$ across the jet shear layer.

In addition to the Eulerian velocity field, the simulation involves the temporal advancement (time tracking) of a total of 2.5×10^6 particles (tracers). The numerical integration of the trajectory of each particle employs the same temporal advancement scheme used for the Eulerian velocity fields (third-order Runge-Kutta scheme). At each time step the particle velocities are obtained from the three-dimensional (3D) Eulerian grid using a 13-point (TS13) interpolating scheme [15]. Other interpolation schemes were implemented and assessed, including linear, tricubic, and spectral ("exact") interpolation. The algorithm for computing the particle trajectories during the simulation was carefully assessed in several different flows and the TS13 interpolation scheme was chosen due to its balance between accuracy and computational cost, as discussed in Yeung and Pope [15]. More details of the validation procedure can be found in Diogo [16].

C. Conditional Lagrangian statistics

Lagrangian statistics were obtained for the particles as function of the time since they crossed the TNTI. The TNTI was detected using the vorticity norm $\omega = (\omega_i \omega_i)^{1/2}$, where ω_i is the vorticity field as in Bisset *et al*. [17]. The detection threshold was $\omega = 0.7 \frac{U_c}{\delta_{0.5}}$, where U_c is the centerline mean velocity and $\delta_{0.5}$ is the jet half-width, respectively. The chosen threshold is the same used by Bisset *et al*. [17] and Mathew and Basu [5] but this fact alone does not justify the use of the same threshold in a different simulation. Indeed, the exact value of the threshold has to be assessed for each new simulation or experimental data and for this purpose we used the same procedure described in Bisset *et al*. [17], which led to the threshold chosen. Appendix A describes a new "automatic" procedure that can be used to detect this threshold.

To illustrate the shape of the TNTI, Fig. 1 shows a zoom of the TNTI region from the far-field, self-similar region of the jet, defined as an isosurface of constant vorticity norm equal to the detection threshold. The interface exhibits structures shaped as "hills," associated with higher vertical values of the local interface location Y_I, which are separated by "valleys" and trenches (smaller Y_I). In the present simulation the average lateral size of these hills is roughly equal to the Taylor microscale.

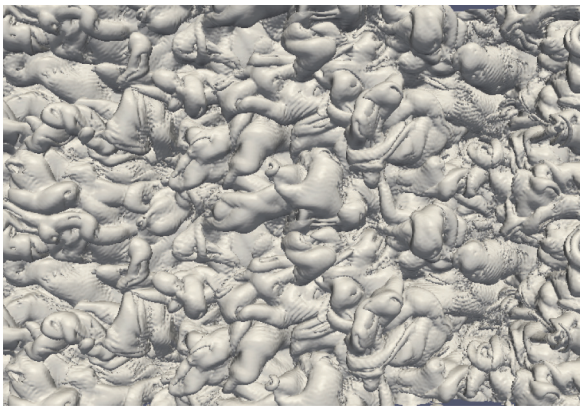

FIG. 1. (Color online) Partial (top) view of the isosurface of the vorticity magnitude defining the TNTI, taken from the self-similar region of the jet.

An innovative aspect of the present work consists in using particles from the irrotational region near the TNTI region and to observe them entering the turbulent region. This approach is more suited to study the entrainment process since the statistics involve the particle trajectories, thus reflecting the distances of the fluid elements to the TNTI during the entrainment process, in contrast with conditional Eulerian statistics used in, e.g., Westerweel *et al*. [6] and da Silva and Pereira [9], where the distances from the TNTI used in the conditional statistics are not the actual distances traveled by the particles during the entrainment process.

The procedure to obtain the Lagrangian statistics starts with the initial seeding of the particles (tracers) once the jet has reached the self-similar turbulent regime. The particles are randomly placed both at the upper and lower irrotational flow region of the jet, at a distance of up to $0.5H$ from the TNTI location. To visualize the evolution of the particle positions as well as their vorticity Figs. 2(a)–2(f) show the position of some particles and their vorticity norm at different instants of the simulation ($t/t_{\mathrm{ref}} = 24.6$, 28.4, 33.2, 37.9, 42.7, and 47.5, respectively) in a (x,y) plane placed at the middle of the computational domain. Figure 2(a) shows the particles at the (initial) time when the particles are seeded in the simulation, while Figs. 2(b)–2(f) show several successive instants from the simulation.

One can see that the majority of particles move towards the center of the jet, although some move away from it, as a consequence of the jet growth. Also, towards the end of the simulation, several particles entrained by the jet display a vorticity magnitude lower than the threshold defining the TNTI

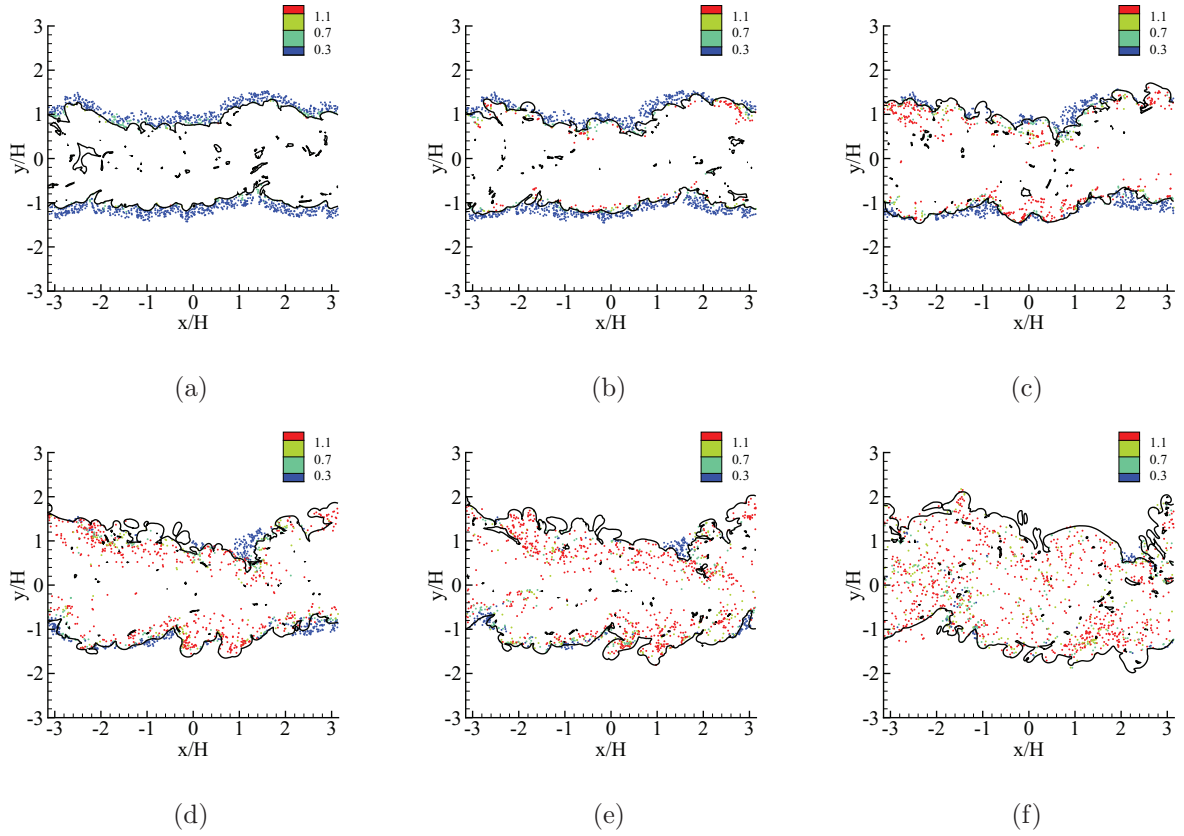

FIG. 2. (Color online) Visualisation of fluid particles location during the simulation in the central plane of the jet (dots) and the TNTI (dark solid line). Each particle corresponds to a dot while the color represents the vorticity norm associated to the particle. Low (high) vorticity corresponds to darker (medium) gray (blue and red), respectively. (a) Initial particle location at the time particles were seeded in the irrotational region of the flow adjacent to the TNTI ($t/t_{\mathrm{ref}} = 24.6$); [(b)–(f)] several consecutive instants during the simulation (from $t/t_{\mathrm{ref}} = 28.4$ to $t/t_{\mathrm{ref}} = 47.5$).

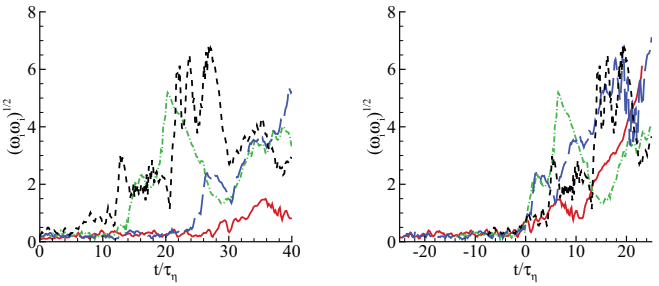

FIG. 3. (Color online) Temporal signals of the vorticity norm, normalized by the velocity of the center line U_c and the jet half-width $\delta_{0.5}$, of four different particles. (a) The "original" signals, and (b) the signals "centered" at the time the particles cross the TNTI.

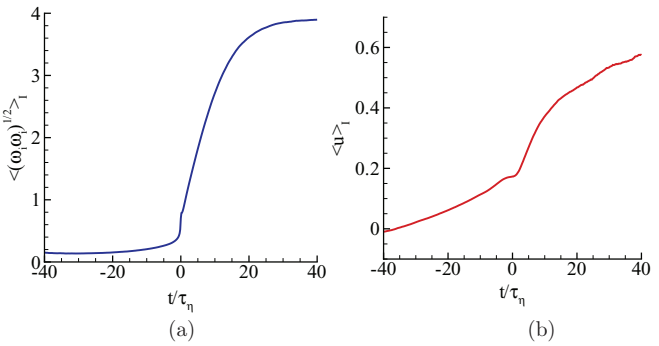

FIG. 4. (Color online) Conditional (a) vorticity and (b) streamwise velocity profile across the turbulent-nonturbulent interface in the planar turbulent jet using Lagrangian statistics. The interface is at $t = 0$, and the irrotational and turbulent regions correspond to $t < 0$ and $t > 0$, respectively.

$(0.7\frac{U_c}{\delta_{0.5}})$, which means that they are trapped inside irrotational fluid "bubbles" which were entrained into the jet by large-scale engulfing.

For instance, the particles located at $(x/H, y/H) = (1,1)$ in Fig. 2(b) seem to be "engulfed" into the turbulent region of the jet in the subsequent images [Figs. 2(c)–2(f)]. Nevertheless, the amount of particles entrained through this process seems to be low compared with the global amount of particles entering the jet. This agrees with Basu [5] in the sense that this process provides a relatively small contribution to the total entrainment in the jet. One can also observe that these particles move increasingly faster in the streamwise direction as they acquire significant velocity still in the irrotational region.

For the Lagrangian statistics only particles that cross the TNTI and become part of the turbulent flow region are selected for the analysis. For this purpose one has to compute the exact location of the TNTI along the entire simulation. As stated before we define the instantaneous TNTI location using a vorticity magnitude isosurface with a threshold given by $\omega = 0.7\frac{U_c}{\delta_{0.5}}$ [5,17], which is computed during the simulation using the instantaneous values of U_c and $\delta_{0.5}$. For each particle trajectory we define t^0 as the time when a particle crosses the computed TNTI location, the time series of a given quantity is centred at $t = 0$ using this reference time, i.e., t becomes $t - t^0$. Figures 3(a) and 3(b) illustrate the procedure for four individual particles showing their vorticity temporal signals (normalized by the centerline velocity and jet half-width) before [Fig. 3(a)] and after [Fig. 3(b)] being reset by the "reference" time, i.e., the time t becomes $t - t^0$, where t^0 is the time when each particle crosses the TNTI.

In the present work the total simulation time since the initial placement of the particles in the vicinity of the jet is about $52\tau_\eta$, where τ_η is the Kolmogorov time. The final averaged conditional Lagrangian enstrophy profile is obtained by averaging the conditional enstrophy time series from the individual particles. Figures 4(a) and 4(b) show the conditional mean Lagrangean enstrophy and streamwise velocity profiles for the present simulation at the far-field (self-similar) region. The TNTI is located at $t = 0$, while the irrotational and turbulent regions correspond to $t < 0$ and $t > 0$, respectively. We label these Lagrangian statistics by $\langle\rangle_I$ to differentiate them from the classical statistics. The conditional mean enstrophy displays a characteristic sharp jump at the TNTI and is roughly constant inside the turbulent region. A similar behavior is observed in conditional Eulerian vorticity statistics e.g., Westerweel *et al.* [6]. The mean thickness of the observed vorticity jump is roughly equal to $20\tau_\eta$, consistent with the 10–15 η observed for the same simulation using Eulerian conditional statistics [14]. The mean conditional Lagrangian streamwise velocity also resembles the corresponding mean conditional Eulerian profile [18]. Specifically, the velocity mean is already important at the TNTI (reaching roughly 1/3 the value inside the turbulent region) and displays a characteristic velocity jump inside the turbulent region, as discussed in, e.g., Westerweel *et al.* [6].

III. LAGRANGIAN ENSTROPHY STATISTICS NEAR THE TURBULENT-NONTURBULENT INTERFACE

A. Enstrophy governing equation

The enstrophy is $\omega_i\omega_i/2$, where the vorticity field ω_i is given as the curl of the velocity vector u_i, i.e., $\omega_i = \varepsilon_{ijk}\partial u_j/\partial x_k$. Its transport equation is written as

$$\frac{D}{Dt}\left(\frac{1}{2}\omega_i\omega_i\right) = \omega_i\omega_j S_{ij} + \nu\frac{\partial^2}{\partial x_j\partial x_j}\left(\frac{1}{2}\omega_i\omega_i\right) - \nu\frac{\partial\omega_i}{\partial x_j}\frac{\partial\omega_i}{\partial x_j}, \quad (1)$$

where ν is the molecular viscosity and $\frac{D}{Dt}$ stands for the total derivative. The terms on the right-hand side represent enstrophy production, viscous diffusion, and viscous dissipation, respectively.

B. Lagrangian mean enstrophy budget near the TNTI

The mean profiles of the terms governing the evolution of the enstrophy across the TNTI are shown in Fig. 5. In the irrotational region $t < 0$ all the terms are negligible while in the turbulent region far away from the TNTI ($t/\tau_\eta > 20$) a balance between enstrophy production and viscous dissipation is observed. The most interesting feature appears close to the TNTI, where, as one approaches the turbulent region from the irrotational flow region, the mean enstrophy viscous diffusion

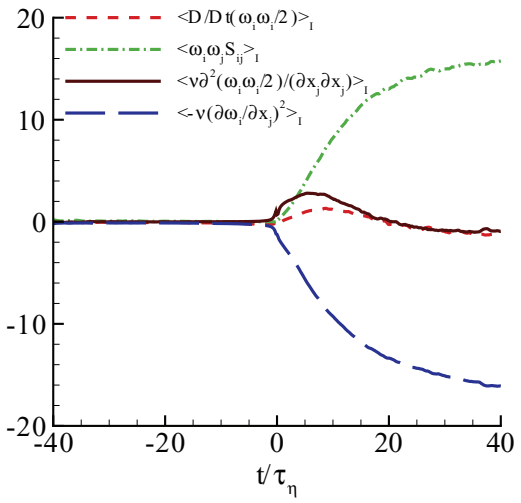

FIG. 5. (Color online) Conditional Lagrangian enstrophy budgets across the turbulent-nonturbulent interface in the planar turbulent jet. The TNTI is at $t = 0$, while the irrotational and turbulent regions correspond to $t < 0$ and $t > 0$, respectively.

is positive and the dominating term, i.e., there exists a small layer at the edge of the irrotational region where (viscous) diffusion is important, whereas enstrophy production and viscous dissipation remain negligible.

This means that this term or mechanism, although integrating to zero for the whole computational domain, drives the growth of the total enstrophy near the TNTI. This agrees with the classical ideas about the mechanisms behind turbulent entrainment as described in Corrsin and Kistler [2], i.e., the entrainment process is indeed triggered by viscous diffusion of enstrophy from the turbulent region. A similar result has been observed in experimental data from an oscillating grid [10] and direct numerical simulations of a turbulent planar jet [11] where conditional mean (Eulerian) profiles of enstrophy diffusion exhibit a similar positive or negative contribution near the TNTI. Also in agreement with this, it has been observed in experimental data from a turbulent jet that the probability density function of the enstrophy transport near the jet edge is symmetrical and yields a zero mean value for enstrophy flux [6].

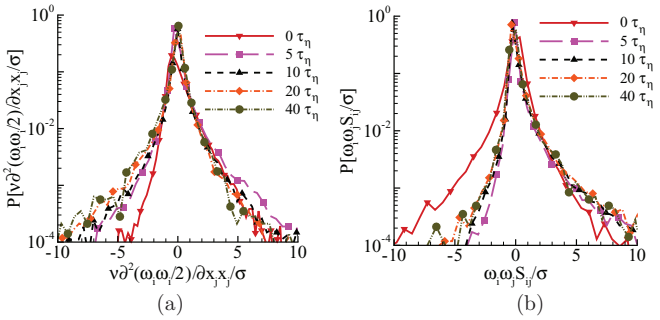

FIG. 6. (Color online) Lagrangian probability density functions (PDFs) of the enstrophy viscous diffusion (a) and enstrophy production (b), taken at several instants from the reference time where the particles cross the TNTI ($t = 0$).

C. Lagrangian probability density functions near the TNTI

Figures 6(a) and 6(b) show the probability density functions (PDFs) of the enstrophy viscous diffusion and enstrophy production, respectively, normalized by their variance and centered at their mean value, at several instants from the reference time they cross the TNTI. Inspection of the figures shows that the diffusion is roughly symmetric inside the turbulent region (for $t/\tau_\eta > 5$) and positively skewed near the TNTI due to the positive contribution to the growth of enstrophy described before. On the other hand, the production is positively skewed inside the turbulent region and slightly negatively skewed at the TNTI. This suggests a predominance of enstrophy production by vortex stretching versus compression inside the core of the jet and the slight predominance of vortex compression at the TNTI as documented in da Silva and Pereira [9]. For $t/\tau_\eta > 10$ the PDFs of each term collapse, indicating that the influence of the TNTI is no longer felt, i.e., the terms already display their "turbulent" behavior.

D. Lagrangian joint probability density functions across the TNTI

A deeper look into the mechanisms responsible for the transport of enstrophy from the turbulent into the nonturbulent (irrotational) region can be achieved by analyzing the joint probability density functions (JPDFs) of enstrophy variation and the terms responsible for the main enstrophy increase near the TNTI: viscous enstrophy diffusion and enstrophy production.

Figures 7(a)–7(d) show the JPDFs of the enstrophy variation and enstrophy production at several instants. In the irrotational region [$t/\tau_\eta = -5$; Fig. 7(a)] and at the TNTI [$t/\tau_\eta = 0$; Fig. 7(b)] no correlation can be observed between the two quantities. The enstrophy production seems to have no role on the enstrophy increase at these locations. On the other hand, inside the turbulent region [$t/\tau_\eta \geqslant 5$; Figs. 7(c) and 7(d)] the two quantities are clearly correlated: For $t/\tau_\eta \geqslant 5$ it is evident that the enstrophy production causes the enstrophy local value to increase.

Figures 8(a)–8(d) show the JPDF of the enstrophy variation and the enstrophy viscous diffusion. In contrast with the observed enstrophy production, (viscous) diffusion is already felt outside the turbulent region as attested by Fig. 8(a) from $t/\tau_\eta = -5$ showing already some degree of correlation between the diffusion and temporal variation. The correlation level increases significantly at the TNTI [Fig. 8(b) from $t/\tau_\eta = 0$], particularly for positive values of both quantities (not for negative values), clearly demonstrating that the enstrophy growth is caused by the viscous diffusion, while inside the turbulent region the correlation between these quantities is less clear [Figs. 8(c) and 8(d) from $t/\tau_\eta \geqslant 5$].

E. Densities in the (R, Q) plane across the TNTI

Since the work of Chong *et al.* [19] and Cantwell [20] considerable attention has been given to the invariants of the velocity gradient tensor $A_{ij} = \partial u_i/\partial x_j$. In incompressible flows this tensor has only two nonzero invariants, the second

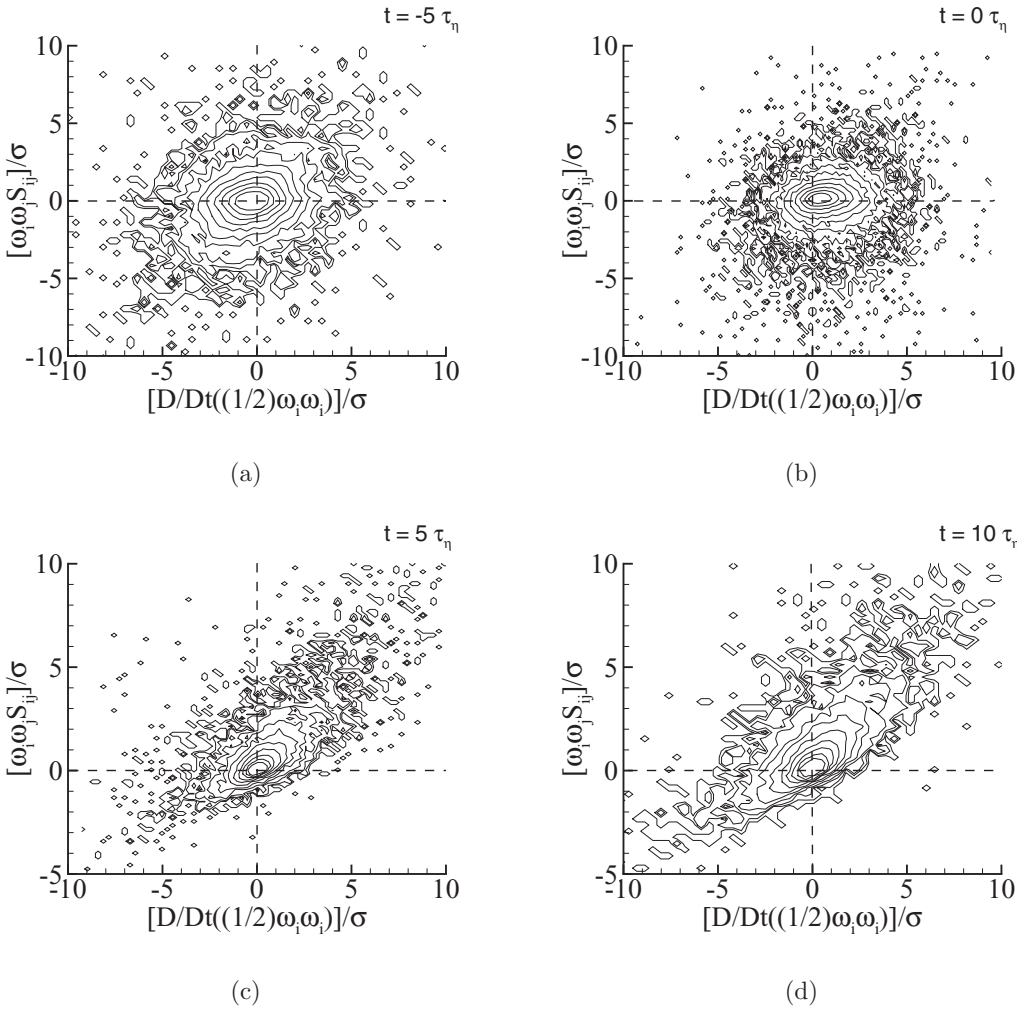

FIG. 7. Lagrangian joint probability density functions (JPDFs) of enstrophy total variation and enstrophy production taken at several instants from the reference time where the particles cross the TNTI ($t = 0$). The irrotational and turbulent regions correspond to $t < 0$ and $t > 0$, respectively: (a) $t/\tau_\eta = -5$, (b) $t/\tau_\eta = 0$, (c) $t/\tau_\eta = +5$, and (d) $t/\tau_\eta = +10$.

Q and third R, defined by

$$Q = -\tfrac{1}{2}A_{ij}A_{ji} = \tfrac{1}{4}(\omega_i\omega_j - 2S_{ij}S_{ij}) \tag{2}$$

and

$$R = -\tfrac{1}{3}A_{ij}A_{jk}A_{ki} = -\tfrac{1}{3}\left(S_{ij}S_{jk}S_{ki} + \tfrac{3}{4}\omega_i\omega_j S_{ij}\right), \tag{3}$$

respectively.

It is important to recall the physical meaning of these invariants (see Davidson [21], Ooi *et al*. [22], Blackburn *et al*. [23], and Soria *et al*. [24]). If $Q > 0$, enstrophy is more important than strain product, whereas if $Q < 0$ the opposite occurs. In a Burgers vortex flow, for instance, the center of the vortex is characterized by $Q > 0$, while in the region around it $Q < 0$, implying that strain product (and, hence, the viscous dissipation of the kinetic energy) dominates.

The meaning of R depends on the sign of Q. If $Q \gg 0$, then $R \sim -1/4\omega_i\omega_j S_{ij}$ and $R < 0$ implies a predominance of vortex stretching over vortex compression, while if $Q \ll 0$, then $R \sim -1/3S_{ij}S_{jk}S_{ki} = -3\alpha_S\beta_S\gamma_S$, where $\alpha_S \geqslant \beta_S \geqslant \gamma_S$ are the three eigenvalues of S_{ij} arranged in descending order. Due to incompressibility, $\alpha_S + \beta_S + \gamma_S = 0$, therefore $R > 0$ implies that $\alpha_S, \beta_S > 0; \gamma_S < 0$, and the associated flow structure is sheetlike, whereas $R < 0$ implies a tube like structure.

In order to assess at which locations in the (R, Q) invariant phase space, the enstrophy governing mechanisms take place it is interesting to analyze density functions of the enstrophy viscous diffusion and enstrophy production in the (R, Q) map across the TNTI. As in Chertkov *et al*. [25], van der Bos *et al*. [26], and Wang *et al*. [27], we define the density function (DF) of a given flow quantity Φ by

$$\Phi(R,Q) = \int \Phi P(R,Q,\Phi)d\Phi = P(R,Q)\langle\Phi|R,Q\rangle, \tag{4}$$

where $P(R, Q, \Phi)$ is the joint PDF of the R and Q invariants and the variable Φ, while $\langle\Phi|R, Q\rangle$ is the conditional average of Φ. The enstrophy production density, for instance, is defined by

$$\begin{aligned}\omega_i\omega_j S_{ij}(R,Q) &= \int \omega_i\omega_j S_{ij} P(R,Q,\omega_i\omega_j S_{ij})d\omega_i\omega_j S_{ij} \\ &= P(R,Q)\langle\omega_i\omega_j S_{ij}|R,Q\rangle.\end{aligned} \tag{5}$$

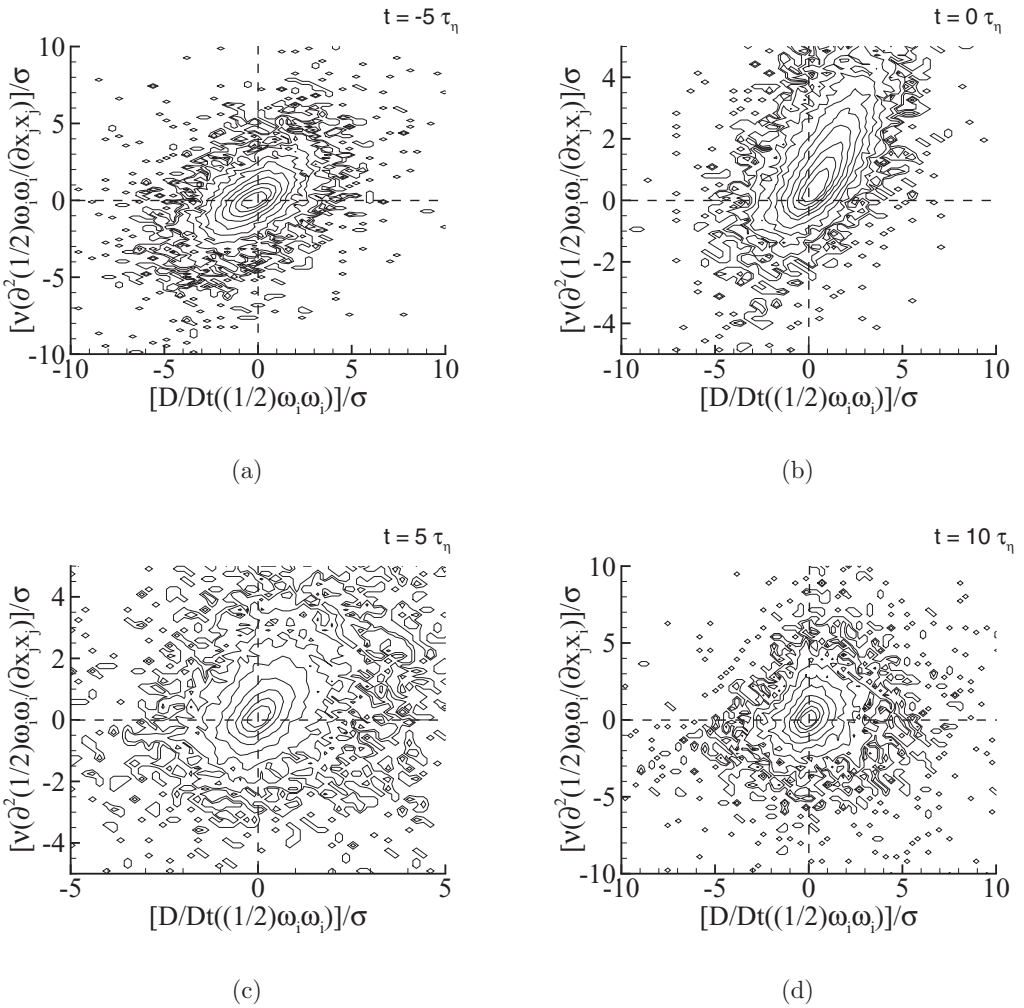

FIG. 8. Lagrangian joint probability density functions (JPDFs) of enstrophy total variation and enstrophy viscous diffusion taken at several instants from the reference time where the particles cross the TNTI ($t = 0$). The irrotational and turbulent regions correspond to $t < 0$ and $t > 0$, respectively: (a) $t/\tau_\eta = -5$, (b) $t/\tau_\eta = 0$, (c) $t/\tau_\eta = +5$, and (d) $t/\tau_\eta = +10$.

Figures 9(a)–9(c) show DF plots of enstrophy production, i.e., $P(R,Q)\langle\omega_i\omega_j S_{ij}|R,Q\rangle$ at several instants. The figures show no appreciable difference for $t/\tau_\eta = 0$ (TNTI), $t/\tau_\eta = 10$, and $t/\tau_\eta = 20$, being also very similar to the figures in Chertkov *et al.* [25] and van der Bos *et al.* [26].

Enstrophy production due to vortex stretching takes place either in regions where enstrophy is more important than strain product and where vortex stretching is more important than vortex compression ($R < 0, Q > 0$) and also in regions of biaxial strain ($R > 0, Q < 0$). Negative enstrophy production,

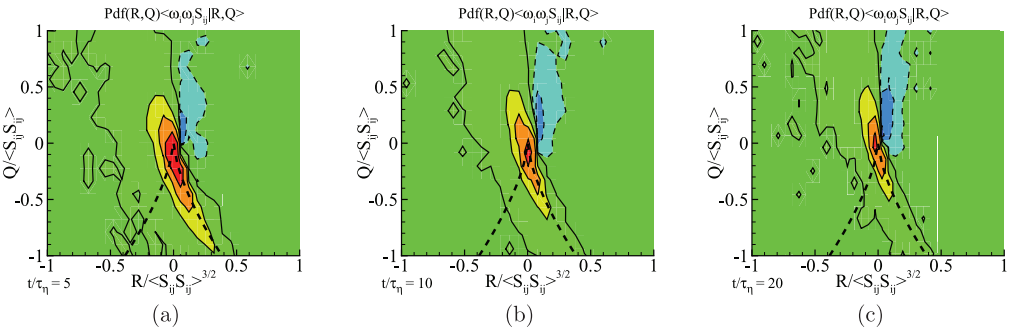

FIG. 9. (Color online) Enstrophy production density $P(R,Q)\langle\omega_i\omega_j S_{ij}|R,Q\rangle$ at several instants in relation to the time when particles cross the TNTI ($t = 0$) for the present simulation: (a) $t/\tau_\eta = 0$, (b) $t/\tau_\eta = 10$, and (c) $t/\tau_\eta = 20$. Negative contours are represented by dotted lines and darker (stronger colors) represent higher magnitudes.

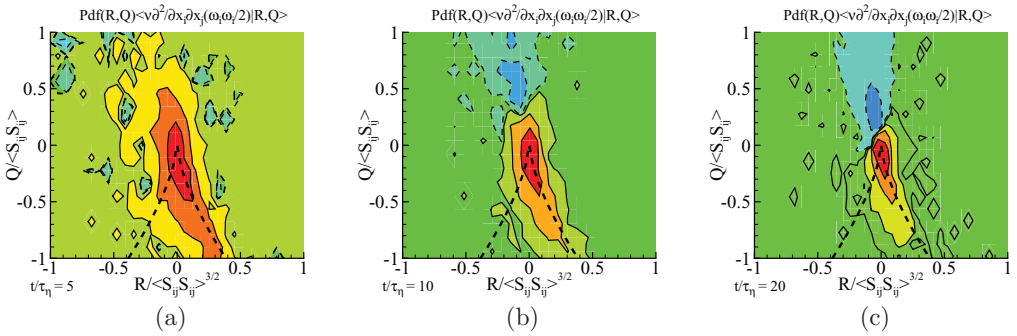

FIG. 10. (Color online) Enstrophy viscous diffusion density $P(R,Q)\langle \nu \frac{\partial^2}{\partial x_j \partial x_j}(\frac{1}{2}\omega_i\omega_i)|R,Q\rangle$ at several instants in relation to the time when particles cross the TNTI ($t=0$) for the present simulation: (a) $t/\tau_\eta = 0$, (b) $t/\tau_\eta = 10$, and (c) $t/\tau_\eta = 20$. Negative contours are represented by dotted lines and darker (stronger colors) represent higher magnitudes.

on the other hand, occurs in regions of vortex compression ($R>0, Q>0$). At the TNTI positive enstrophy production, which as we saw before is negligible at this location, occurs preferentially in regions of biaxial strain ($R>0, Q<0$), whereas enstrophy attenuation due to vortex compression occurs in regions of axial compression ($R<0, Q<0$).

The DFs of enstrophy viscous diffusion $P(R,Q)$ $\langle \nu \frac{\partial^2}{\partial x_j \partial x_j}(\frac{1}{2}\omega_i\omega_i)|R,Q\rangle$ are displayed in Figs. 10(a)–10(c). Inside the turbulent region for $t/\tau_\eta > 10$ [Figs. 10(b) and 10(c)] positive values of enstrophy viscous diffusion are obtained mainly in flow regions where strain product is more important than enstrophy ($Q<0$), whereas negative values of the diffusion term occur in flow regions where enstrophy is more important than strain ($Q>0$). This result is not surprising since it is known that enstrophy is mainly concentrated in long-lived vortex tubes which are surrounded by regions where strain product and kinetic energy dissipation dominate. This seems to imply that the enstrophy viscous diffusion tends to decrease the level of enstrophy at the core of the vortex tubes and to transport this enstrophy towards regions surrounding the tubes. At the TNTI ($t/\tau_\eta = 0$), on the other hand, the density of the enstrophy viscous diffusion exhibits a very different behavior [Fig. 10(a)]. Here enstrophy viscous diffusion is positive both above and below the "Vieillefosse" lines. Indeed, it is difficult to see where the very small negative values of this term lie in the (R,Q) map. This shows that the enstrophy viscous diffusion is a source of enstrophy where fluid particles are entrained at the TNTI for all possible topologies within the R,Q map.

IV. ANALYSIS OF THE PARTICLE TRAJECTORIES DURING THE ENTRAINMENT

A. Number of particles trapped inside "irrotational bubbles"

In this section we analyze the amount of particles that find their way into the shear layer ending up inside irrotational bubbles that exist in the turbulent region. The existence of these bubbles is a consequence of the "engulfment" flow mechanism and several of these bubbles can be observed in two-dimensional cuts of the shear layer, e.g., one of such bubbles is located at $(x/H, y/H) \approx (0, -0.8)$ in Fig. 2(c). The number of particles entrained into irrotational bubbles can be used to estimate the relative importance between "nibbling" and "engulfing" in the planar turbulent jet. Engulfing is a large-scale process that proceeds into two stages: (i) an inviscid first stage, where regions of irrotational flow are drawn into the core of the shear layer, which is followed by (ii) the swallowing of these pockets (or bubbles) by a viscous-dominated process acting at their edges. The existence of an appreciable number of particles (initially seeded at the vicinity of the TNTI) inside these bubbles would clearly indicate that "engulfing" plays a major role in the turbulent entrainment process. Conversely, if this number is small, "engulfing" is not important for the present flow.

In the present simulation and using the vorticity magnitude threshold the flow field was divided into three different regions. Regions where the vorticity exceeded the threshold were deemed as being part of the turbulent region, whereas the ones below the threshold were defined as being irrotational. A distinction was made between the irrotational fluid region outside the TNTI and the pockets of irrotational fluid imprisoned inside the turbulent envelope. For the latter, the label of *irrotational bubbles* was given.

The procedure to detect these irrotational bubbles uses common connectivity algorithms (see Shapiro and Accman [28]) to analyze whether a flow point below the defined vorticity magnitude threshold is surrounded by points labeled as "turbulent," i.e., whether they are inside an irrotational bubble or outside the shear layer. Details of this procedure are given in Appendix B. Notice that some flow regions appear to be also irrotational bubbles when depicted from a two-dimensional cut through the shear layer but turn out to be connected to the irrotational flow region. We label these "apparent" irrotational bubbles as *irrotational 2D bubbles*.

Figure 11(a) shows the total number of points labeled as irrotational bubbles defined using the procedure described in Appendix B during the simulation (since the time the particles were inserted outside the turbulent region). The total number of points labeled as irrotational bubbles seems to be slowly oscillating during the simulation but is always quite small, e.g., always less than $\approx$1.5% of the flow points inside the turbulent region are termed "irrotational."

To analyze how many particles are trapped into these small regions of irrotational fluid we tracked the position of individual particles randomly placed both at the upper and

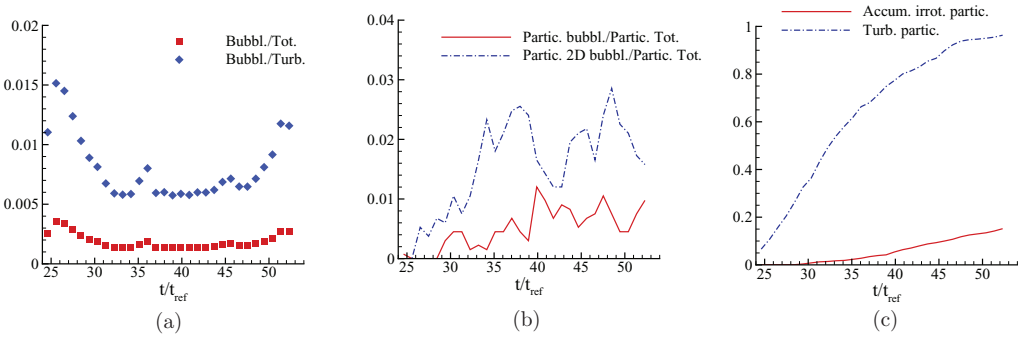

FIG. 11. (Color online) (a) Total number of points labeled as irrotational found inside the turbulent region (Bubbl.) divided by the total number of points of the computational domain (Tot.) and by the total number of points labeled as turbulent (Turb.). (b) Number of particles found inside the irrotational bubbles (Partic. bubbl.) divided by the total number of particles (Partic. Tot.) ("2D bubbl." stands for 2D irrotational bubbles). (c) Total number of particles that were once inside an irrotational bubble (Accum. irrot. partic.) and the total number of particles that are inside the turbulent region (Turb. partic.); both numbers are normalized by the number of instantaneous particles inside the turbulent region.

lower shear layers of the jet, up to a distance of $0.5H$ from the TNTI location in a single (x, y) plane placed at the middle of the computational domain [Figs. 2(a)–2(f), described previously, show the position of these particles at several snapshots during the simulation].

Figure 11(b) shows the total number of particles that end up inside the irrotational bubbles during the simulation divided by the total number of particles. "2D bubbl." represents the 2D irrotational bubbles. The number of particles captured inside an irrotational bubble oscillates strongly during the simulation but is always quite small, e.g., less than 1% of the total number of particles. The fraction of particles trapped inside the "apparent" (irrotational 2D bubbles) is a bit higher but remains also quite small (less than ≈3.0%).

Figure 11(c) shows the total number of particles that are inside the turbulent region excluding particles inside the irrotational bubbles (Turb. partic.) and the total number of particles that were once inside irrotational bubbles (Accum. irrot. partic.). Both numbers are normalized by the total number of particles inside the turbulent region. As can be seen the total number of particles trapped inside the bubbles is small compared to the total number of particles in the turbulent region.

These results suggest that "engulfing" is not important for the present flow. A more detailed study of the geometry and evolution of these bubbles should be the subject of another study, e.g., it would be interesting to make a similar study in different flows to see whether, as suggested by Phillip and Marusic [7], engulfment is more important in jets than in wakes.

B. Particle motion in relation to the TNTI location

In order to analyze the dispersion of the particles during the entrainment process, Figs. 12(a) and 12(b) show statistics of the vertical distance of each particle to the TNTI during the simulation δy_p. For each instant of the simulation this distance was taken both for the particles entering at the upper and lower shear layers. When the distance is zero the particles are at the TNTI location while negative and positive values of δy_p represent distances to the TNTI taken for particles in the turbulent or irrotational region, respectively. Given the small amount of particles that end up in the irrotational bubbles, no effort was made to separate these particles from particles inside the shear layer in regions of turbulent motions.

The mean distance to the TNTI is displayed in Fig. 12(b) and decreases in time as the particles are drawn into the turbulent

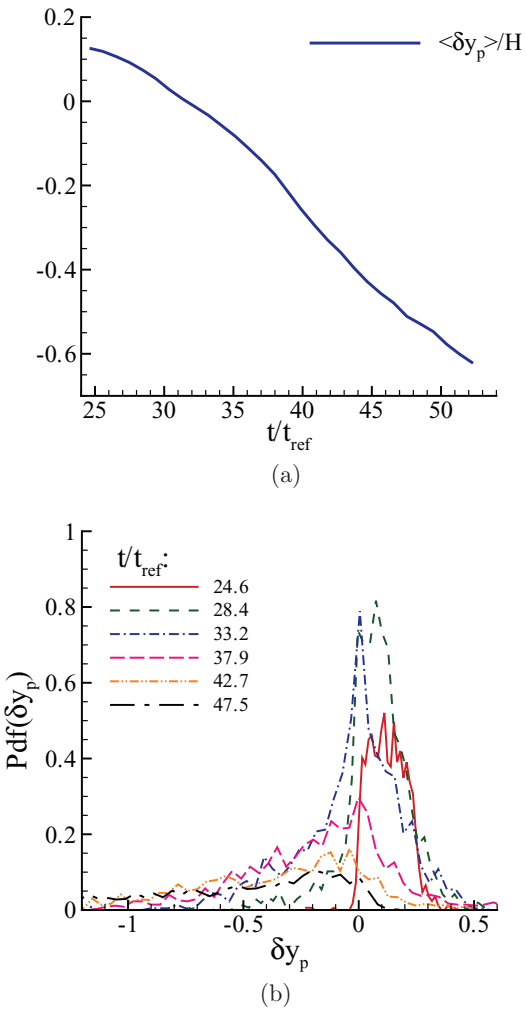

FIG. 12. (Color online) (a) Mean vertical distance of the particles to the location of the TNTI δy_p. (b) Probability density function (PDF) of the vertical distance of the particles to the location of the TNTI δy_p.

region. It is interesting to see that the particles continue to move into the jet center long time after they have been entrained. A mean velocity could be computed from the slope of δy_p and the figures shows that this speed is a bit slower near the TNTI than far away from it.

The PDFs of δy_p for several instants are displayed in Fig. 12(b). Initially, for $t/t_{\text{ref}} = 24.6$, the particles are equally distributed with the distance from the TNTI, as expected. After some time, however, the particles tend to accumulate near the TNTI as observed by the shape of the PDF of δy_p at $t/t_{\text{ref}} = 33.2$. This suggests that the entrainment velocity and the entrainment process itself near the TNTI proceeds at a slower pace compared to away from the TNTI. For later instants ($t/t_{\text{ref}} = 42.7$), most of the particles have already been entrained inside the shear layer and one observes that the PDFs of δy_p become "flat" again, indicating that the entrained particles disperse at several distances from the interface some time after the entrainment has taken place, suggesting a comparatively free motion of the particles inside the turbulent region.

The results suggest that the entrainment of particles involves a relatively slow motion near the TNTI than elsewhere. This is consistent with the existence of a entrainment phase associated with viscous processes at the TNTI. Alternatively, this may imply that the particles move in a direction which is approximately tangent to the TNTI position once this interface has been crossed. The shape of the streamlines of the flow near the TNTI as displayed in, e.g., Bisset *et al.* [17] is consistent with this hypothesis. By moving tangent to the TNTI the fluid elements have enough time to build up their vorticity content before they are pushed further into the interior of the shear layer.

V. CONCLUSIONS

A DNS of a temporal plane jet at $\text{Re}_\lambda \approx 110$ was used to study the dynamics of the enstrophy during the turbulent entrainment process which is present in many free shear flows such as mixing layers, wakes, and jets. Specifically, 2.5 millions of particles (tracers) initially seeded outside the jet (in the irrotational region) near the TNTI were tracked along the simulation, allowing the detailed study of the enstrophy generation during their entrainment into the turbulent shear layer. The innovative aspect of this study consists in analyzing the entrainment using Lagrangian statistics, where the distances from the TNTI location express the trajectories of fluid elements in the vincinity of the TNTI, which is not the case when using Eulerian conditional statistics.

Lagrangian statistics show the existence of a vorticity jump associated with a length scale which is one order of magnitude greater than the Kolmogorov microscale, in agreement with previous results for Eulerian statistics, e.g., da Silva and Taveira [14]. Moreover, the existence of a streamwise velocity jump described by Westerweel *et al.* [6] is also detected in the Lagrangian statistics.

Analysis of the enstrophy transport terms for the particles along the simulation showed that the turbulent entrainment mechanism starts with a growth of enstrophy in the irrotational near the TNTI caused by the viscous diffusion and is followed by an increase due to enstrophy production that dominates the flow inside the turbulent region. Probability density functions of the enstrophy diffusion and production show that these mechanism change substantially from the TNTI to inside the core of the turbulent region, e.g., enstrophy diffusion is negatively skewed at the TNTI and not inside the turbulent region, where it leads to no net increase of the enstrophy, whereas enstrophy production is only perceived by fluid particles after the TNTI region has been crossed into the turbulent region. Density functions of the enstrophy governing terms in the (R, Q) map allowed the detailed study of the topology of the terms acting on the particles during the entrainment.

Finally, we analyzed the importance of the "engulfment" mechanism for the present jet, using information from the tracked particles and their relation to the "irrotational bubbles" originated from the engulfment motions. The analysis showed that the volume from these "irrotational bubbles" accounts for less than 1.5% of the turbulent volume of the jet and that only less than 1% of the particles initially placed outside the shear layer end up inside these bubbles. Probability density functions of particle position in relation to the TNTI position show that the particles spend more time crossing the region near the TNTI than traveling inside the turbulent region, consistent with the particles moving tangent to the interface around the time they cross it. The results suggests that the "engulfment" mechanism is not important for the entrainment for the present jet, in agreement with previous numerical and experimental works [3,5].

APPENDIX A: DETECTION OF THE TNTI

The TNTI can be seen as a (zero-thickness) surface separating turbulent from irrotational flow and can be defined in terms of vorticity versus no-vorticity content of the flow. Several methods have been used to detect the TNTI in several different flows, e.g., Bisset *et al.* [17] and Westerweel *et al.* [6]. Many of these methods consist in looking for a low vorticity-magnitude threshold ω_{tr}, below which flow regions can be considered to be (approximately) irrotational. A difficulty arises due to the existence of perturbations within the irrotational flow (in experimental data) or numerical noise (in numerical simulations) that prevent the use of a straightforward approach to detect this threshold. A useful observation is that there is a vorticity magnitude range where statistics of the interface layer, e.g., conditional vorticity profiles in relation to the distance from the TNTI, as well as the geometric shape of the interface layer itself, are weakly dependent on the vorticity magnitude threshold.

Bisset *et al.* [17] computed conditional vorticity profiles from a numerically simulated wake and found that for vorticity magnitude thresholds near $\omega_{\text{tr}} = 0.7U_0/\delta$, where U_0 and δ are the velocity deficit and shear layer thickness, respectively, the conditional vorticity magnitude and the TNTI geometry changes little. Therefore, this threshold could be used to define the location of the TNTI for the simulated wake.

Figures 13(a) and 13(b) show the volume of the turbulent region for the present jet, as function of the vorticity magnitude threshold used to detect it $\text{Vol}_T = \text{Vol}(\omega > \omega_{\text{tr}})$. For a range of vorticity magnitudes there is a plateau of turbulent volume between $\omega_{\text{tr}} \approx 0.08(U_1/H)$ to $\omega_{\text{tr}} \approx 0.30(U_1/H)$, and using

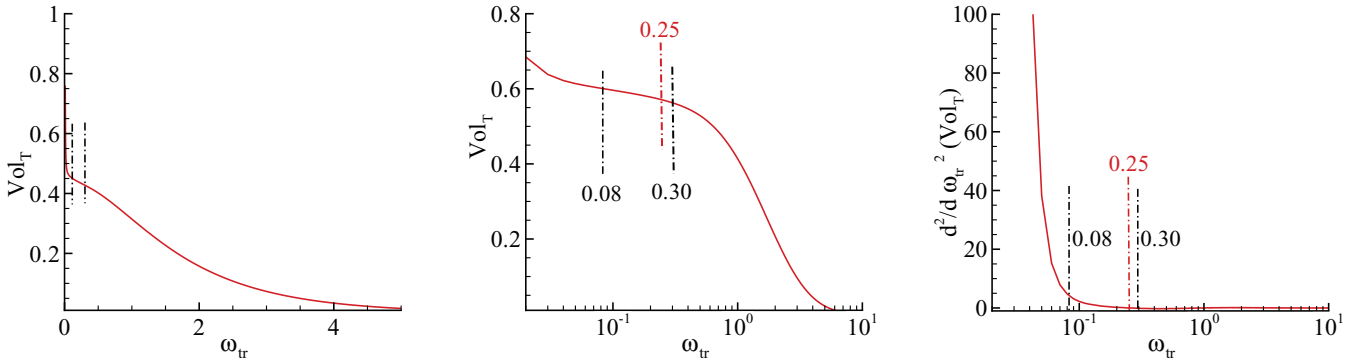

FIG. 13. (Color online) (a) Volume of the vorticity region as function of the vorticity magnitude for an instantaneous vorticity field. There is a plateau between $\omega_{tr} = 0.08U_1/H$ and $\omega_{tr} = 0.30U_1/H$, where the volume of the vorticity (or turbulent) region changes very slowly with the vorticity magnitude (threshold). Any value within this plateaulike region could be used to define the TNTI (or, alternatively, the vorticity magnitude threshold defining the TNTI is within this plateau). (b) Same as (a) but in linear-log coordinates and zoomed over the region of interest. (c) Second derivative of the turbulent volume with the identification of the detected threshold (point where second derivative intersects zero).

any value of vorticity magnitude comprised within this plateau to detect or define the location of the TNTI leads to similar geometry of the TNTI and similar conditional statistics.

In the present work we employ an automatic method to determine a vorticity magnitude threshold within this plateau. The method is inspired by the observed change in the curvature of $\mathrm{Vol}_T = \mathrm{Vol}_T(\omega_{tr})$, from convex to concave, displayed in Fig. 13(a). The vorticity threshold used to locate the TNTI ω_{tr} is defined by the inflexional point, i.e., the point where the second derivative of the volume of the turbulent region is zero,

$$\omega_{tr} : \frac{\partial^2 \mathrm{Vol}_T}{\partial \omega_{tr}^2} = 0. \tag{A1}$$

In the present case this value is $\omega_{tr} \approx 0.25(U_1/H)$. Figure 13(c) shows the location of the detected threshold in the curve for the second derivative of the turbulent volume.

Figures 14 show the influence of the vorticity magnitude threshold in the location of the TNTI used for its detection for the two values delimiting the plateau of turbulent volume [$\omega_{tr} = 0.08(U_1/H)$ and $\omega_{tr} = 0.30(U_1/H)$]. As can be seen the TNTI location varies weakly for vorticity magnitudes located within this plateaulike region and therefore in practice any value within this range could be used to detect the TNTI.

APPENDIX B: DETECTION OF POCKETS OF IRROTATIONAL FLUID INSIDE THE SHEAR LAYER (IRROTATIONAL BUBBLES)

In order to detect irrotational bubbles, a common connectivity algorithm was used (see Shapiro and Accman [28]). Irrotational bubbles consist of pockets of fluid where the local vorticity magnitude is below the threshold defined as "turbulent" that are surrounded by

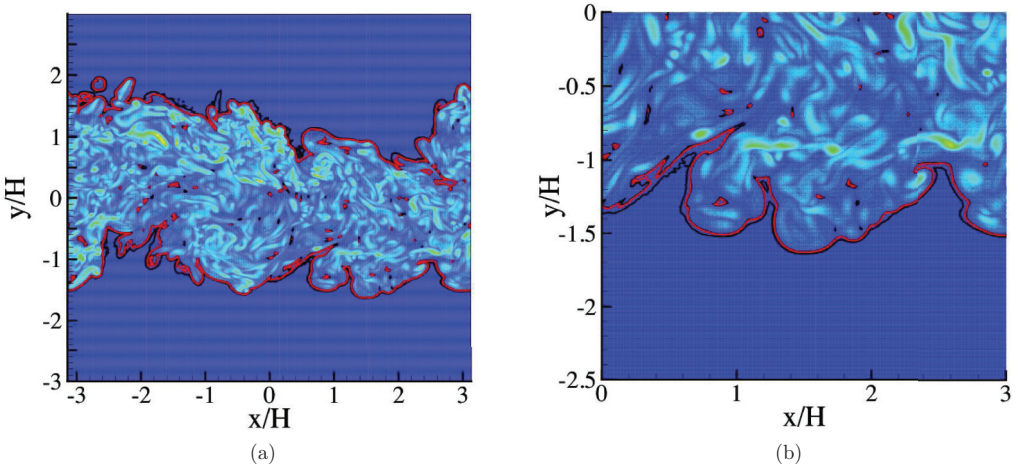

FIG. 14. (Color online) Contours of vorticity magnitude in a side view of the planar jet with lines defining particular vorticity values used to detect the TNTI. The dark (black) lines represent values delimiting the turbulent volume plateau ($\omega_{tr} = 0.08U_1/H$ and $\omega_{tr} = 0.30U_1/H$), and the gray (red) line the particular threshold detected by the automatic method ($\omega_{tr} = 0.25U_1/H$). (a) Side view showing the full domain; (b) zoom showing a region near the jet edge.

flow points labeled as "turbulent," i.e., they consist of fluid pockets that are irrotational while being inside the shear layer.

The employed algorithm [28] starts by applying a simple logical filter to select either irrotational or turbulent regions, i.e., whose enstrophy levels exceed the previously determined threshold. Subsequently, the 3D flow field is partitioned in the spanwise direction into a set of blocks to be treated in parallel. To each block a common two-stage connected neighborhood procedure is used. (i) In the first stage, the algorithm covers each pixel of the box, where a stencil containing the binary test results is interrogated in order to look for the lowest label of each pixel vicinity. If a lower label is found, this is attributed to the pixel or a new incremental label is assigned. For the case of turbulent regions a simple 4-connected neighborhood search is made, using a 7-point stencil, whereas consistency requirements enforce irrotational regions to be built using an 8-connected neighborhood, with a 27-point stencil. (ii) The second stage of the algorithm consists in a reverse bottom-up sweep, where the stencils use the updated first-stage labeled results in order to construct a local equivalence table that contains the information about all connected labels within each individual box. After finishing the construction of all local equivalence tables, the boundaries between the contiguous partitions are evaluated in order to assemble a global equivalence table that conciliates the labels from the entire 3D flow field. Finally, the global equivalence table is used to assign the correct label to each flow region. Furthermore, for the case of the irrotational regions, the blob size and its location serve as an automatic criteria to distinguish the internal nonturbulent bubbles from the external irrotational regions that involve the shear layer.

Some flow regions appear to be also irrotational bubbles when depicted from a 2D cut through the shear layer but turn out to be connected to the irrotational flow region. To analyse these bubbles, an algorithm similar to the one applied to the 3D field is applied to each spanwise 2D slice, planes (x, y). The 2D labels are then compared to the 3D which were previously obtained in order to determine if a given nonturbulent region is part of a 3D irrotational bubble or if it is part of the external irrotational regions that is perceived as an irrotational bubble from a 2D slice of the flow. To the latter one attributes the symbolic classification of *2D irrotational bubble*. Experimental works using 2D cuts through the turbulent region may consider these regions as contributing to the "engulfment" mechanism and arguably some of these bubbles will eventually end up as a closed irrotational region inside the turbulent region. Nevertheless, the number of these events (and their volume) must be taken only as an upper bound for the number of "engulfing" events.

[1] J. S. Turner, J. Fluid Mech. **173**, 431 (1986).
[2] S. Corrsin and A. L. Kistler, Technical Report No. TN-1244, NACA, 1955 (unpublished).
[3] J. Westerweel, C. Fukushima, J. M. Pedersen, and J. C. R. Hunt, Phys. Rev. Lett. **95**, 174501 (2005).
[4] A. A. Townsend, *The Structure of Turbulent Shear Flow* (Cambridge University Press, Cambridge, 1976).
[5] J. Mathew and A. Basu, Phys. Fluids **14**, 2065 (2002).
[6] J. Westerweel, C. Fukushima, J. M. Pedersen, and J. C. R. Hunt, J. Fluid Mech. **631**, 199 (2009).
[7] J. Philip and I. Marusic, Phys. Fluids **24**, 055108 (2012).
[8] M. Holzner, A. Liberzon, N. Nikitin, W. Kinzelbach, and A. Tsinober, Phys. Fluids **19**, 071702 (2007).
[9] C. B. da Silva and J. C. F. Pereira, Phys. Fluids **20**, 055101 (2008).
[10] M. Holzner, A. Liberzon, B. Luthi, N. Nikitin, W. Kinzelbach, and A. Tsinober, J. Fluid Mech. **598**, 465 (2008).
[11] C. B. da Silva and R. J. N. dos Reis, Phil. Trans. R. Soc. A **369**, 738 (2011).
[12] C. B. da Silva, R. J. N. dos Reis, and J. C. F. Pereira, J. Fluid Mech. **685**, 165 (2011).
[13] A. B. Cortesi, B. L. Smith, G. Yadigaroglu, and S. Banerjee, Phys. Fluids **11**, 162 (1999).
[14] C. B. da Silva and R. R. Taveira, Phys. Fluids **22**, 121702 (2010).
[15] P. Yeung and S. B. Pope, J. Comp. Phys. **79**, 373 (1988).
[16] José S. Diogo, Master's thesis, IST/Technical University of Lisbon, 2012.
[17] D. K. Bisset, J. C. R. Hunt, and M. M. Rogers, J. Fluid Mech. **451**, 383 (2002).
[18] R. R. Taveira and C. B. da Silva, Phys. Fluids **25**, 015114 (2013).
[19] M. Chong, E. Perry, and B. Cantwell, Phys. Fluids **2**, 765 (1990).
[20] B. Cantwell, Phys. Fluids **5**, 2008 (1993).
[21] P. A. Davidson, *Turbulence: An Introduction for Scientists and Engineers* (Oxford University Press, Oxford, 2004).
[22] A. Ooi, J. Martin, J. Soria, and M. Chong, J. Fluid Mech. **381**, 141 (1999).
[23] H. Blackburn, N. Mansour, and B. Cantwell, J. Fluid Mech. **310**, 269 (1996).
[24] J. Soria, R. Sondergaard, B. Cantwell, M. Chong, and A. Perry, Phys. Fluids **6**, 871 (1994).
[25] M. Chertkov, A. Pumir, and B. I. Chraiman, Phys. Fluids **11**, 2394 (1999).
[26] F. van der Bos, B. Tao, C. Meneveau, and J. Katz, Phys. Fluids **14**, 2456 (2002).
[27] B. Wang, D. Bergstrom, J. Yin, and E. Yee, J. Turbulence **7**(34), (2006).
[28] L. G. Shapiro and G. Stokman, *Computer Vision* (Prentice Hall, Upper Saddle River, NJ, 2001).